

**FABRICATION AND CHARACTERIZATION OF
BLACK SILICON FOR HETEROJUNCTION
SOLAR CELLS**

AUWAL ABDULKADIR

UNIVERSITI SAINS MALAYSIA

2022

**FABRICATION AND CHARACTERIZATION OF
BLACK SILICON FOR HETEROJUNCTION
SOLAR CELLS**

by

AUWAL ABDULKADIR

**Thesis submitted in fulfilment of the requirements
for the degree of
Doctor of Philosophy**

January 2022

ACKNOWLEDGEMENT

In the name of Allah, the Most Beneficent, the Most Merciful.

All praise and thanks are due to the Almighty ALLAH SUBHANAHU WA'TAALA, the lord of the universe for bestowing me with health, capability, strength, wisdom, and knowledge to complete this PhD thesis. ALHAMDULILLAH.

First and foremost, I would like to express my deep gratitude and appreciation to PVMD research group and my main supervisor Ts. Dr. Mohd Zamir bin Pakhuruddin for his tireless support and guidance during the research, may ALLAH SUBHANAHU WA'TAALA reward him. My appreciation also goes to my co-supervisor Professor Dr. Azlan bin Abdul Aziz for his support and encouragement from day one of my PhD candidature. My sincere appreciation and word of thanks to all staffs in Nano-Optoelectronics Research and Technology Laboratory (NOR Lab). My appreciation and word of thanks also goes to all staffs in Science and Engineering Research Centre (SERC), Engineering Campus of USM. I would like to also thank all faculty members and administrative staffs of School of Physics. Secondly, I would like to thank my beloved wife Aisha Muhammad MAJIGIRI, my children at present (Maryam and Amina) for being supportive and helpful throughout the PhD journey.

Lastly, I would like to thank my mother, guardian father and stepmother Gwaggo Hauwa Adamu for their parental upbringing which indeed reflects in the PhD. I would also like to thank Abubakar Gambo, Mustapha Ibrahim and Hadiza Tukur for always being there for me with love, support, prayers, encouragement, and inspiration which really reflects in the PhD journey.

Auwal Abdulkadir

Penang, Malaysia, January 2022

TABLE OF CONTENTS

ACKNOWLEDGEMENT	ii
TABLE OF CONTENTS	iii
LIST OF TABLES	vi
LIST OF FIGURES	viii
LIST OF SYMBOLS	xix
LIST OF ABBREVIATIONS	xxii
ABSTRAK	xxvi
ABSTRACT	xxviii
CHAPTER 1 INTRODUCTION	1
1.1 Introduction	1
1.2 Problem statement	11
1.3 Objectives.....	13
1.4 Thesis outline	14
1.5 Original contributions	15
CHAPTER 2 LITERATURE REVIEW AND THEORETICAL BACKGROUND	17
2.1 Introduction	17
2.1.1 Light trapping in crystalline silicon solar cells	20
2.1.2 Fabrication of black silicon.....	26
2.1.3 Metal-assisted chemical etching (MACE)	27
2.1.3(a) One-step MACE process	28
2.1.3(b) Two-step MACE process	30
2.1.4 Hybrid (microtextures/nanotexture) texturing of crystalline silicon.....	34
2.1.5 Heterojunctions black silicon solar cells.....	35

2.2	Theoretical background	41
2.2.1	Solar radiation	42
2.2.2	Theoretical background on crystalline silicon solar cells	43
2.2.3	N-Type c-Si.....	46
2.2.4	P-Type c-Si	47
2.2.5	P-N junction solar cell.....	47
	2.2.5(a) Short-circuit current (J_{sc})	49
	2.2.5(b) Open-circuit voltage (V_{oc}).....	51
	2.2.5(c) Fill factor (FF)	51
	2.2.5(d) Efficiency (EFF)	52
2.2.6	Theoretical background on black silicon (Graded refractive index model)	52
CHAPTER 3 METHODOLOGY.....		57
3.1	Introduction	57
3.2	Fabrication of black silicon	57
3.2.1	One-step MACE process.....	61
3.2.2	Two-step MACE process	62
3.2.3	Hybrid (microtextures/nanotextures) texturing of crystalline silicon	64
3.3	Characterization of black silicon.....	65
3.3.1	Atomic Force Microscopy (AFM)	65
3.3.2	Field Emission Scanning Electron Microscopy (FESEM)	67
3.3.3	UV-Vis-NIR spectrophotometer	69
3.4	Fabrication of heterojunction black silicon solar cells.....	71
3.4.1	Heterojunction emitter based on transparent oxides	71
3.4.2	Heterojunction emitter based on organic material	73
3.4.3	Thermal evaporation of front Ag and rear Al contacts	74
3.4.4	Hall effect measurements.....	77

3.5	Characterization of heterojunction black silicon solar cells.....	78
3.5.1	Solar simulator	79
CHAPTER 4 RESULTS AND DISCUSSIONS		81
4.1	Introduction	81
4.2	Black silicon based on one-step MACE process.....	81
4.2.1	Effect of etching time.....	81
4.2.2	Effect of HF concentration.....	87
4.3	Black silicon based on two-step MACE process.....	94
4.3.1	Effect of etching time.....	94
4.3.2	Effect of Ag NPs layer thickness	100
4.3.3	Effect of HF concentration.....	111
4.3.4	Effect of H ₂ O ₂ concentration	117
4.4	Black silicon based on hybrid (micro/nano) texturing of crystalline silicon..	123
4.4.1	Effect of one-step MACE process	124
4.4.2	Effect of two-step MACE process	130
4.5	Heterojunction solar cells based on transparent oxide emitter.....	143
4.5.1	Effect of transparent oxide thin-film thickness.....	144
4.5.2	Effect of post-deposition annealing of transparent oxide thin film	160
4.6	Heterojunction solar cells based on organic emitter	175
CHAPTER 5 CONCLUSIONS AND RECOMMENDATIONS.....		188
5.1	Conclusions	188
5.2	Recommendations	190
REFERENCES.....		192
LIST OF PUBLICATIONS		

LIST OF TABLES

	Page
Table 2.1	Literature status of MACE-based b-Si: Synthesis methods, etchants composition, etching time, nanotexture types, length of nanotextures WARs and EFF achieved. 18
Table 3.1	Experimental conditions and measurements done for b-Si fabricated using one-step MACE. 62
Table 3.2	Experimental conditions and measurements done for b-Si fabricated using two-step MACE at fixed H ₂ O ₂ concentration. 63
Table 3.3	Experimental conditions and measurements done for b-Si fabricated using two-step MACE at fixed HF concentration. 64
Table 4.1	Properties of b-Si fabricated using two-step MACE under different Ag NPs deposition time. 108
Table 4.2	Summary of morphological and optical properties of b-Si nanowires fabricated on both n-type c-Si and p-type c-Si using the same etching conditions. 110
Table 4.3	Properties of b-Si fabricated using two-step MACE under different H ₂ O ₂ concentration. 120
Table 4.4	NaOH etch time, MACE etch time and WARs of hybrid b-Si fabricated using one-step MACE with different pyramids' sizes 130
Table 4.5	NaOH etch time, MACE etching conditions and WARs of hybrid b-Si fabricated using two-step MACE with different pyramids' sizes 134
Table 4.6	Summary of morphological and optical properties of hybrid textures fabricated on both n-type c-Si and p-type c-Si using same etching conditions. 142

Table 4.7	Summary of morphological feature sizes and WAR from b-Si fabricated using different MACE processes on n-type and p-type c-Si.	142
Table 4.8	EDX (wt.%) of sputtered ITO thin films on b-Si nanowires.	150
Table 4.9	EDX (wt.%) of ITO thin film on b-Si nanowires annealed at different temperatures.	165
Table 4.10	Hall effect results (sheet resistance, carrier concentration and carrier mobility) of 300 nm ITO on b-Si after annealing at different temperatures.	170
Table 4.11	Hall effect measurements of PEDOT:PSS on c-Si, b-Si and hybrid textured surfaces.....	181
Table 4.12	PV parameters for heterojunction solar cells featuring PEDOT:PSS organic emitter on c-Si, b-Si and hybrid textured surfaces.....	184

LIST OF FIGURES

		Page
Figure 1.1	NREL solar cell efficiency chart [2]	2
Figure 1.2	Schematic images of: (a) planar reference c-Si, (b) nanotextured and (c) hybrid textured wafers [15].....	3
Figure 1.3	Light trapping mechanisms in: (a) nanotextured and (b) hybrid microtextures/nanotextures b-Si [24,25].....	5
Figure 1.4	C-Si solar cells; (a) Al-BSF homojunction (b) TCO/p-type c-Si heterojunction and (c) DASH heterojunction solar cell concept [26,28,29].....	7
Figure 1.5	Energy band diagram of DASH solar cell featuring TMOs under short-circuit condition. The TMOs form heterojunctions with c-Si at the opposite ends and provide selective contacts for holes and electrons, respectively. Components of dark, tunnelling and thermionic emission currents are identified on the band diagram. The diagram is not drawn to scale.	10
Figure 1.6	(a) Total reflection and absorption of planar c-Si within 300-1100 nm wavelength region (b) Planar c-Si (c) B-Si [34].....	11
Figure 2.1	Top (a) and cross section (b) FESEM images of pyramidally textured c-Si using NaOH texturing. The scale bar is with 5 μm and 1 μm respectively [62].....	21
Figure 2.2	Nucleation of Ag ⁺ (a), Ag NPs growth with local oxidation of c-Si to SiO ₂ (b), Ag NPs trapped into the pits (initial pits formation) (c), vertical moving of the grown Ag NPs (dendrites) deeper into c-Si (d) (adopted from [75]).....	30
Figure 2.3	Reduction of H ₂ O ₂ at Ag NPs surface and simultaneous oxidation of c-Si beneath the Ag NPs (a), continuous oxidation and dissolution of c-Si underneath the Ag NPs leading to the formation of vertical b-Si nanowires (b) (adopted from [75]).....	33

Figure 2.4	Top (a) and cross-section (b) FESEM image of Hybrid (microtextures/nanowires) textured c-Si using NaOH and one-step MACE texturing [95].	35
Figure 2.5	Schematic diagram of an n-ZnSe/p-type b-Si heterojunction solar cell (adopted from [105]).	37
Figure 2.6	Schematic diagram of band-alignment in DASH heterojunction solar cells (adopted from [119]).	39
Figure 2.7	AM1.5G standard solar spectrum (spectral irradiance as function of wavelength), AM0 spectrum direct part of the AM1.5G spectrum. Plotted data is available at National Renewable Energy Laboratory (NREL) original data file [125] and the insert image (for AM 0, AM 1 and AM 1.5) was adopted from Newport company website [126].	43
Figure 2.8	Two-level system showing photon absorption only at certain energy (wavelength) level (a-e) with an increasing number of energy levels (horizontally) for direct bandgap material like GaAs. The colour of arrows represents colour of absorbed light, while (f) is band structure of c-Si (indirect bandgap material). (adopted from [129]).	45
Figure 2.9	Schematic of p-n junction showing motion of mobile electrons and holes due to diffusion and the “built-in” electric field [128].	48
Figure 2.10	Electrical circuit of a solar cell showing generated photon current in parallel with p-n-junction diode and a shunt resistor, and in series with another resistor (a) and current density-voltage characteristic curves of solar cell under illumination and in the dark (b) (adopted from [29]).	50
Figure 2.11	Light trapping b-Si nanotextures fabricated by one-step MACE, the scale bar is with 2 μm and 200 nm for the inset (adopted from [24]).	53

Figure 3.1	Diamond Scriber (Model type; RV129) of the Nano-Optoelectronics Research and Technology Laboratory (NOR) USM.	58
Figure 3.2	Flow chart for the fabrication of b-Si and b-Si heterojunction solar cells.	60
Figure 3.3	Image and schematic diagram of Atomic force microscope (AFM) [136].	66
Figure 3.4	Image and schematic diagram of working principle of field emission scanning electron microscopy (FESEM) (model: FEI Nova NanoSEM 450) [137].	68
Figure 3.5	Image and schematic diagram of working principle of UV-Vis-NIR spectroscopy (Agilent Carry 5000; schematic is adopted from [138]).	70
Figure 3.6	Schematic diagrams of reference c-Si heterojunction solar cell; (a) using ITO emitter and NiO hole contact and (b) PEDOT:PSS/c-Si solar cell.	72
Figure 3.7	The image and schematic diagram of direct current and radiofrequency (DC/RF) magnetron sputtering system (Edwards Auto 500 model) used in NOR lab USM (schematic image adopted from [139]).	73
Figure 3.8	The image of spin coater and schematic diagram of PEDOT:PSS spin coating process (schematic image adopted from [140]).	74
Figure 3.9	Image of Ag contacted b-Si solar cell. Dimensions of the stainless-steel shadow mask used to make the front contacts are indicated.	75
Figure 3.10	Image and schematic diagram of thermal evaporation system (Edwards Auto 306 model).	76
Figure 3.11	Blue furnace used for metal contact annealing in NOR Lab School of Physics, USM.	76

Figure 3.12	Image and schematic diagram of Hall effect measuring system; model: LAKESHORE CONTROLLER 601/DRC-93CA (the schematic is adapted from [141]).....	78
Figure 3.13	Photograph image showing sample b-Si heterojunction solar cell for Hall effect measurements.	78
Figure 3.14	Photograph image and schematic diagram of LED based light source solar simulator (model: TMS-2X2 Forter Technology).	79
Figure 3.15	White LED, Compact Fluorescent (CFL) and Incandescent bulbs Spectra. AM1.5G standard solar spectrum is shown for comparison [144].	80
Figure 4.1	Reference c-Si (a), (b) 60 s (c) 70 s (d) 80 s (e) 90 s etched b-Si using one step AgNO ₃ -based MACE process.	82
Figure 4.2	Oblique (30°) and top view of b-Si nanowires with different etching duration; (a and e) 60 s, (b and f) 70 s, (c and g) 80 s, (d and h) 90 s. The scale bar is 1 μm in length.....	83
Figure 4.3	Cross-sectional FESEM images of b-Si nanowires with different etching duration; (a) 60 s (b) 70 s (c) 80 s (d) 90 s. The scale bar is 1 μm in length.	84
Figure 4.4	(a) Reflection curves for b-Si wafers etched at different etching times. Reference c-Si (planar) is used for comparison. (b) Absorption curves for b-Si wafers etched at different etching times.	85
Figure 4.5	Length of b-Si nanowires (primary y-axis) and corresponding WAR (secondary y-axis) after being etched at different etching duration.	87
Figure 4.6	Top and oblique (30°) view of b-Si nanowires fabricated with different HF concentration; (a and b) 2.5 M, (c and d) 7.5 M, (e and f) 10.0 M, (g and h) 12.5 M. The scale bar is 1 μm in length.	88
Figure 4.7	Cross sectional SEM of b-Si nanowires fabricated with different HF concentration at 80s; (a) 2.5 M (b) 7.5 M (c) 10.0 M (d) 12.5	

	M. The scale bar is 1 μm in length for (a), (b) and 5 μm in length for (c), (d).....	89
Figure 4.8	Schematic diagram showing favoured etching directions of c-Si: (a) under low HF concentration and (b) under high concentration of HF. The diagram is not drawn to scale.	91
Figure 4.9	Reflectance curves for b-Si wafers etched with different HF concentration (a) Absorption curves for b-Si wafers etched with different HF concentration (b). Reference c-Si (planar) is used for comparison.	92
Figure 4.10	Length of b-Si nanowires (primary y-axis) and corresponding WAR (secondary y-axis) after being etched at different HF Concentration.	93
Figure 4.11	Top and oblique (30°) SEM images of b-Si nanowires produced using different etching duration; (a and b) 10 s, (c and d) 15 s, (e and f) 20 s, (g and h) 25 s. The scale bar is 1 μm in length.	96
Figure 4.12	Cross-sectional SEM images of b-Si nanowires produced using different etching duration: (a) 10 s (b) 15 s (c) 20 s (d) 25 s. The scale bar is 1 μm in length.....	97
Figure 4.13	AFM images of b-Si nanowires produced using different etching times (a) 10 s (b) 15 s (c) 20 s (d) 25 s.....	98
Figure 4.14	Reflection curves for b-Si wafers etched at different etching times (a), Absorption curves for b-Si wafers etched at different etching times (b). For both curves, reference c-Si (planar) is used for comparison.	99
Figure 4.15	Length of b-Si nanowires (primary y-axis) and corresponding WAR (secondary y-axis) after being etched at different etching duration.	100
Figure 4.16	Top oblique (30°) and cross-sectional FESEM images of Ag NPs layers with different thicknesses on c-Si produced using different deposition durations; (a and e) 10 s (thickness $\sim 1.3 \mu\text{m}$), (b and f) 20 s (thickness $\sim 2.6 \mu\text{m}$), (c and g) 30 s (thickness $\sim 5.1 \mu\text{m}$), (d	

	and h) 40 s (thickness $\sim 1.5 \mu\text{m}$). The scale bar is $1 \mu\text{m}$ in length for top oblique (30°) images and $3 \mu\text{m}$ in length for the cross-sectional FESEM images.	101
Figure 4.17	Top oblique (30°) FESEM and cross-sectional FESEM images of 20 s etched b-Si nanowires produced using Ag NPs layers with different thicknesses; (a and e) 250 nm, (b and f) 322 nm, (c and g) 577 nm, (d and h) 437 nm. The scale bar is $1 \mu\text{m}$ in length.....	103
Figure 4.18	AFM images of b-Si nanowires produced using different Ag NPs layer thicknesses (followed with 20 s etching time); (a) $1.3 \mu\text{m}$ (b) $2.6 \mu\text{m}$ (c) $5.1 \mu\text{m}$ (d) $1.5 \mu\text{m}$	104
Figure 4.19	Reflection curves for b-Si nanowires etched at 20 s etching time with different Ag NPs layer thicknesses (a), Absorption curves for b-Si nanowires etched at 20 s etching time with different Ag NPs layer thicknesses (b). For both curves, reference c-Si (planar) is used for comparison.	105
Figure 4.20	Length of b-Si nanowires (primary y-axis) and corresponding WAR (secondary y-axis) after etching c-Si wafers with different Ag NPs layer thicknesses at 20 s etching duration.	107
Figure 4.21	Top, oblique (30°) FESEM and cross-sectional FESEM, 3D AFM images of 20 s etched b-Si nanowires replicated on n-type c-Si with $5.1 \mu\text{m}$ Ag NPs layer thicknesses. The scale bar is $1 \mu\text{m}$ in length.	109
Figure 4.22	Reflection curves (a), Absorption curves (b); for b-Si nanowires on n-c-Si and p-type c-Si both etched at 20 s etching time with $5.1 \mu\text{m}$ Ag NPs layer thicknesses. For both curves, reference p-type c-Si (planar) is used for comparison.....	110
Figure 4.23	Top, oblique (30°) FESEM images of b-Si nanowires etched with different HF concentrations; (a and b) 3.52 M, (c and d) 10.56, (e and f) 14.08 M, (g and h) 17.60 M. The scale bar is $1 \mu\text{m}$ in length.	112

Figure 4.24	Cross-sectional FESEM images of b-Si nanowires etched with different HF concentrations; (a) 3.52 M, (b) 10.56, (c) 14.08 M, (d) 17.60 M. The scale bar is 1 μm in length.....	113
Figure 4.25	3D AFM images of b-Si nanowires etched with different HF concentrations: (a) 3.52 M, (b) 10.56, (c) 14.08 M, (d) 17.60 M. ...	115
Figure 4.26	Reflection (a), Absorption (a): of b-Si nanowires etched with different HF concentrations; 3.52 M, 10.56 M, 14.08 M, 17.60 M.	116
Figure 4.27	Top, oblique (30 ^o) FESEM images of b-Si nanowires etched with different H ₂ O ₂ concentrations; (a and b) 0.62 M, (c and d) 1.85, (e and f) 2.47 M, (g and h) 3.7 M. The scale bar is 1 μm in length.	118
Figure 4.28	Cross-sectional FESEM images of b-Si nanowires etched with different H ₂ O ₂ concentrations; (a) 0.62 M, (b) 1.85, (c) 2.47 M, (d) 3.7 M. The scale bar is 1 μm in length.....	119
Figure 4.29	3D AFM images of b-Si nanowires etched with different H ₂ O ₂ concentrations: (a) 0.62 M, (b) 1.85 M, (c) 2.47 M, (d) 3.7 M.....	122
Figure 4.30	Reflection curve (a), Absorption curve (b): of b-Si nanowires etched with different H ₂ O ₂ concentrations; 0.62 M, 1.85 M, 2.47 M, 3.7 M.....	122
Figure 4.31	WAR (primary y-axis) and corresponding length of b-Si nanowires (secondary y-axis) after being etched at different H ₂ O ₂ Concentration.	123
Figure 4.32	(a) 25 min (top view) (b) 25 min (cross-section) (c) 30 min (top view) (d) 30 min (cross-section) (e) 35 min (top view) (f) 35 min (cross-section) (g) 40 min (top view) (h) 40 min (cross-section). The scale bar for all images is 5 μm in length.	124
Figure 4.33	AFM images; (a) 25 min NaOH (b) 30 min NaOH (c) 35 min NaOH (d) 40 min NaOH.	126
Figure 4.34	Reflection curves for microtextured wafers textured at different times (a), Absorption curves for microtextured wafers textured at different times (b). For both curves, reference c-Si (planar) is used for comparison.	126

Figure 4.35	Images of hybrid textures via 80 s one-step MACE; (a) 25 min NaOH and MACE (top) (b) 25 min NaOH and MACE (cross-section) (c) 30 min NaOH and MACE (top) (d) 30 min NaOH and MACE (cross-section) (e) 35 min NaOH and MACE (top) (f) 35 min NaOH and MACE (cross-section) (g) 40 min NaOH and MACE (top) (h) 40 min NaOH and MACE (cross-section). The scale bar for all images is 4 μm in length.....	128
Figure 4.36	Reflection (a), Absorption (b): curves of hybrid textures with b-Si nanowires on the pyramids being fabricated via one-step MACE; 25 min NaOH and 80s MACE, 30 min NaOH and 80s MACE, 35 min NaOH and 80s MACE, 40 min NaOH and 80s MACE. Planar c-Si is used for reference in both curves.	129
Figure 4.37	Images of hybrid textures with b-Si nanowires being fabricated via two-step MACE; (a) A: 25 min NaOH and MACE (oblique) (b) A: 25 min NaOH and MACE (cross-section) (c) B: 30 min NaOH and MACE (oblique) (d) B: 30 min NaOH and MACE (cross-section) (e) C: 35 min NaOH and MACE (oblique) (f) C: 35 min NaOH and MACE (cross-section) (g) D: 40 min NaOH and MACE (oblique) (h) D: 40 min NaOH and MACE (cross-section). The scale bar for all images is 4 μm in length.	131
Figure 4.38	AFM images; (a) A: 25 min NaOH and MACE (b) B: 30 min NaOH and MACE (c) C: 35 min NaOH and MACE (d) D: 40 min NaOH and MACE.	132
Figure 4.39	Reflection curves of sample A (25 min NaOH and MACE), B (30 min NaOH and MACE), C (35 min NaOH and MACE) and D (40 min NaOH and MACE) (a), Absorption curves of sample A (25 min NaOH and MACE), B (30 min NaOH and MACE), C (35 min NaOH and MACE) and D (40 min NaOH and MACE) (b). For both curves, reference c-Si is used for comparison.....	133
Figure 4.40	Top and cross-section FESEM images of hybrid textures E, F, G and H fabricated via two-step MACE: (a) and (b); 30 s and 10 s,	

	(c) and (d); 30 s and 20 s, (e) and (f); 30 s and 30 s, (g) and (h); 30 s and 40 s. The scale bar for all images is 4 μm in length.	135
Figure 4.41	AFM Images of Hybrid textures via two-step MACE; (a) E: NaOH and 30s vs 10s MACE (b) F: NaOH and 30s vs 20s MACE (c) G: NaOH and 30s vs 30s MACE (d) H: NaOH and 30s vs 40s MACE.	138
Figure 4.42	Reflection (a), Absorption (b): curves of hybrid textures with b-Si nanowires being fabricated via two-step MACE; E: NaOH and 30 s and 10 s MACE, F: NaOH and 30 s and 20 s MACE, G: NaOH and 30 s and 30 s MACE, H: NaOH and 30 s and 40 s MACE. Planar c-Si is used for reference in both curves.	139
Figure 4.43	FESEM and AFM images of micro/hybrid textured (NaOH and two-step MACE) on n-type c-Si wafer (a) pyramids top (b) pyramids cross-section (c) hybrid top (d) hybrid cross-section (e) pyramids AFM (f) hybrid AFM. The scale bar for FESEM images is 4 μm in length.....	140
Figure 4.44	Reflection (a), Absorption (b) curves for hybrid textures on: n-type b-Si compared to p-type b-Si. Planar c-Si is used as a reference.....	141
Figure 4.45	Total reflection, transmission and parasitic absorption of bare borosilicate glass (a), (b) Total reflection and transmission (c) Parasitic absorption at ITO/glass interface calculated using; $A=(100-R-T)\%$ (d) Tauc plot; for 50 nm, 80 nm, and 140 nm ITO on glass.....	145
Figure 4.46	Top view and cross section of (a and b) 50 nm ITO on c-Si, (c and d) 80 nm ITO on c-Si, (e and f) 140 nm ITO on c-Si. The scale bar for all images is 400 nm in length.....	148
Figure 4.47	Oblique (30°) and cross section of (a and b) 50 nm ITO on b-Si nanowires (c and d) 80 nm ITO on b-Si nanowires (e and f) 140 nm ITO on b-Si nanowires. The scale bar of all images is with 1 μm length.	149

Figure 4.48	EDX elemental mapping of selected areas for b-Si nanowires and ITO/b-Si nanowires interface; (a) 50 nm ITO (b) 80 nm ITO (c) 140 nm ITO. The scale bar is 250 μm in length.	150
Figure 4.49	AFM images of b-Si nanowires (prior to ITO deposition) and ITO/b-Si nanowires with different ITO thicknesses; (a) b-Si nanowires (b) 50 nm ITO (c) 80 nm ITO (d) 140 nm ITO.	152
Figure 4.50	Reflection and absorption curves of 50 nm, 80 nm, and 140 nm ITO on; (a) c-Si reference (b) b-Si nanowires.	152
Figure 4.51	Carrier mobility (primary y-axis) and sheet resistance (secondary y-axis) with different carrier concentrations (x-axis), for ITO thin film with different thicknesses (50 nm, 80 nm, and 140 nm) on b-Si nanowires.	154
Figure 4.52	Rear interface of; (a) c-Si/NiO/Al (b) b-Si/NiO/Al. The scale bar is 1 μm in length.....	157
Figure 4.53	EDX elemental mapping of selected areas for (a) c-Si/NiO/Al and (b) b-Si/NiO/Al interfaces.....	158
Figure 4.54	Current-voltage characteristics of the non-annealed ITO/b-Si/NiO and ITO/c-Si/NiO reference solar cells measured under the illumination of 47 mW/cm^2 at 25°C (using LED-based solar simulator).	159
Figure 4.55	XRD patterns for 300 nm-thick ITO thin films on b-Si after being annealed at different temperatures (200-500°C).	162
Figure 4.56	Oblique (30°) and cross-section FESEM images of 300 nm ITO thin film on b-Si nanowires after being annealed at different temperatures: (a and b) 200°C (c and d) 300°C (e and f) 400°C (g and h) 500°C. The scale bar is 1 μm in length.	164
Figure 4.57	EDX images of highly magnified selected area of 300 nm ITO thin film on b-Si nanowires after annealing at different temperatures; (a) 200°C (b) 300°C (c) 400°C (d) 500°C. The scale bar is 500 nm in length.....	165

Figure 4.58	AFM images of 300 nm ITO thin film on b-Si after being annealed at different temperature: (a) 200°C (b) 300°C (c) 400°C (d) 500°C.	167
Figure 4.59	(a) Reflection and (b) absorption curves for 300 nm ITO thin film on b-Si nanowires after 200°C, 300°C, 400°C and 500°C post-deposition annealing.....	169
Figure 4.60	Current-voltage characteristics of the ITO/b-Si/NiO and ITO/c-Si/NiO reference solar cells measured under illumination of 47 mW/cm ² at 25°C (using LED-based solar simulator).	172
Figure 4.61	PEDOT:PSS on glass; (a) Reflection, absorption and transmission curves (b) optical bandgap.	176
Figure 4.62	Top, oblique (30°) FESEM images of PEDOT:PSS deposited on; ((a) and (b)) c-Si, ((c) and (d)) b-Si nanowires and ((e) and (f)) hybrid textures. The scale bar is with 1 μm for ((a) and (b)), ((c) and (d)) and with 4 μm for ((e) and (f)).	178
Figure 4.63	AFM images of PEDOT:PSS deposited on; (a) b-Si nanowires and (b) hybrid textures.	179
Figure 4.64	Reflection (a), Absorption (b): curves of PEDOT:PSS deposited on b-Si nanowires and hybrid textures. PEDOT:PSS deposited on c-Si is used as reference.	179
Figure 4.65	Ag contact on: PEDOT:PSS/b-Si nanowires (a), and PEDOT:PSS/hybrid textures (b). The scale bar is 1 μm for (a) and with 4 μm for (b) in length.....	181
Figure 4.66	Current-voltage characteristics of PEDOT:PSS/b-Si, PEDOT:PSS/hybrid textures, and PEDOT:PSS/c-Si reference solar cells: (a) under illumination of 47 mW/cm ² at 25°C (using LED-based solar simulator) and (b) under dark condition.....	182
Figure 4.67	Energy band diagram at PEDOT:PSS/c-Si interface. The diagram is not to the correct scale to make clear band alignment at the interface [198].	183

LIST OF SYMBOLS

D	Absorber thickness
α	Absorption coefficient
E_a	Activation energy
$S(\lambda)$	AM1.5G solar spectrum
E_g	Bandgap
Φ_{SBH}	Barrier height
θ	Bragg's angle or light incidence angle
V_{bi}	Build-in potential
P	Concentration of etchants
D	Crystallite size
J_c	Current density of cathodic process
J_D	Dark current density
$^\circ$	Degrees
$^\circ C$	Degree Celsius
E	Electric field
Q	Electron
x_{Si}	Electron affinity
n_e	Electron carrier concentration
μ_e	Electron carrier mobility
N_s	Electron Density
V	Electron velocity
eV	Electron volt
ν	Frequency
β	Full width at half maximum
R_H	Hall coefficient

V_H	Hall Voltage
n_p	Hole carrier concentration
μ_p	Hole carrier mobility
N	Ideality factor
B	Magnetic field
B_z	Magnetic induction
P_{max}	Maximum power generated
$J_{sc(max)}$	Maximum short-circuit-current density
M	Moles per liter
N_2	Nitrogen
Z	Number of electrons transferred
Ω	Ohms
V_{oc}	Open-circuit voltage
C_{ox}	Oxidant concentration
O	Oxygen
$\%$	Percentage
$h\nu$	Photon energy
h	Planck's constant
P_{in}	Power of light photon per area (1000 W/m ² at standard conditions)
K_c	Reaction rate constant
N	Refractive index
$R(\lambda)$	Reflection
J_o	Reverse saturation current density
S	Seconds
R_s	Series resistance
R_{sheet}	Sheet resistance
K	Shape constant

J_{sc}	Short-circuit current density
R_{sh}	Shunt resistance
T	Thin-film thickness
T	Transmission
V	Volt
λ	Wavelength
Φ_o	Work function of pristine PEDOT:PSS

LIST OF ABBREVIATIONS

AZO	Aluminum doped zinc oxide
Al ₂ O ₃	Aluminum oxide
NH ₄ OH	Ammonium hydroxide
ARCs	Antireflection coatings
AFM	Atomic Force Microscope
ALD	Atomic layer deposition
b-Si	Black silicon
b-Si nanowires	Black silicon nanowires
BZO	Boron doped zinc oxide
CO ₂	Carbon dioxide
CSCs	Carrier selective contacts
CuAl _x	Chalcopyrite
CB	Conduction band
CPD	Contact potential difference
Cu	Copper
Cu(NO ₃) ₂	Copper nitrate
CuO _x	Copper oxide
c-Si	Crystalline silicon
DI H ₂ O	Deionized water
DOS	Density of states
DMSO	Dimethyl sulfoxide
DC	Direct current
DASH	Dopant-free asymmetric heterocontacts

EQE	External quantum efficiency
FESEM	Field Emission Scanning Electron Microscope
FOM	Figure of merit
FF	Fill factor
FWHM	Full width at half maximum
GaAs	Gallium arsenide
Triton X-100	Polyethylene glycol tert-octylphenyl ether
HOMO	Highest occupied molecular orbital
HCL	Hydrochloric acid
HF	Hydrofluoric acid
H ₂ O ₂	Hydrogen peroxide
In	Indium
ITO	Indium tin oxide
IZO	Indium zinc oxide
IBC	Interdigitated back contact
IQE	Internal quantum efficiency
IPA	Isopropanol
LED	Light emitting diode
LCDs	liquid crystal displays
LiF	Lithium fluoride
LOMO	Lowest un-occupied molecular orbital
MgO _x	Magnesium oxide
MACE	Metal-assisted chemical etching
μA	Microampere
μm	Micrometer

ml	Milliliter
min	Minutes
MoO _x	Molybdenum oxide
Nm	Nanometer
NPs	Nanoparticles
NiO	Nickel oxide
HNO ₃	Nitric acid
(NO ₃) ⁻	Nitric ions
Ω cm	Ohm centimeter
OLEDs	Organic light-emitting diodes
PL	Photoluminescence
PV	Photovoltaic
PVMD	Photovoltaics Materials and Devices
PEDOT: PSS	Poly(3,4-ethylenedioxythiophene)–poly(styrene sulfonate)
KOH	Potassium hydroxide
EFF	Power conversion efficiency
RCA	Radio Cooperation of America
RF	Radio frequency
RIE	Reactive ion etching
RMS	Root mean square
c-Si	Silicon
SiN _x	Silicon nitride
SiO ₂	Silicon oxide
Ag	Silver
Ag ⁺	Silver ions

Ag NPs	Silver nanoparticles
AgNO ₃	Silver nitrate
NaOH	Sodium hydroxide
TaN _x	Tantalum nitride
Ta ₂ O ₅	Tantalum pentoxide
TaO _x	Tantalum oxide
HAuCl ₄	Tetra chlorauric acid
TMAH	Tetramethylammonium hydroxide
Sn	Tin
TiO ₂	Titanium oxide
TMO	Transition metal oxides
TCO	Transparent conductive oxides
WO ₃	Tungsten trioxide
UV-Vis-NIR	Ultraviolet visible near infrared
VB	Valence band
V ₂ O ₅	Vanadium pentoxide
H ₂ O	Water
WAR	Weighted average reflectance
ZnSe	Zinc selenide
ZnO	Zinc oxide

FABRIKASI DAN PENCIRIAN SILIKON HITAM UNTUK SEL SURIA HETERO-SIMPANG

ABSTRAK

Silikon hitam (b-Si) adalah teknologi yang menjanjikan pengurangan pantulan jalur lebar dalam rantau jarak gelombang 300-1100 nm dan peningkatan penyerapan cahaya dalam silikon kristal (c-Si). B-Si terdiri daripada permukaan dengan nanowayar rawak atau gabungan nanowayar dan mikrotekstur (tekstur hibrid) yang membawa kepada kesan penggredan indeks refraktif di antara muka udara/c-Si. Dalam karya ini, punaran kimia berbantu logam tanpa elektrod (MACE) digunakan untuk memfabrikasi b-Si. MACE satu-langkah, MACE dua-langkah dan hibrid tekstur-mikro/tekstur-nano digunakan untuk mengkaji pelbagai kesan yang berbeza seperti masa punaran, kepekatan bahan punaran, ketebalan lapisan nanopartikel perak (Ag NPs) ke atas morfologi permukaan dan sifat optik (dalam 300-1100 nm rantau jarak gelombang) b-Si dijalankan. MACE dua-langkah melibatkan masa celup $\text{AgNO}_3:\text{HF}$ yang lebih pendek. Tekstur hibrid melibatkan punaran awal dalam NaOH untuk menghasilkan piramid. Untuk MACE satu-langkah, nanowayar dengan panjang purata $\sim 2.9 \mu\text{m}$ dan diameter purata $\sim 120 \text{ nm}$ ditunjukkan. Pantulan purata wajaran (WAR) sebanyak 6.0% telah direalisasikan. Untuk MACE dua-langkah, nanowayar dengan panjang purata 577 nm dan diameter $\sim 200 \text{ nm}$ dihasilkan dengan WAR $\sim 5.5\%$. Untuk tekstur hibrid, nanowayar dengan panjang antara 450-600 nm telah diperolehi di atas piramid dengan lebar tapak 3-12 μm dan ketinggian 3-8 μm . Nanowayar mempunyai lebar lateral 30-40 nm. WAR $\sim 7.2\%$ diperolehi. Untuk fabrikasi sel suria, b-Si jenis-p digunakan untuk sel suria hetero-simpang berasaskan ITO/b-Si dan b-Si jenis-n

digunakan untuk sel suria hetero-simpang berasaskan PEDOT:PSS/b-Si. Pencirian arus-voltan sel suria dijalankan di bawah simulator suria berasaskan LED cahaya putih (panjang gelombang 400-800 nm) dengan intensiti pencahayaan 47 mW/cm^2 pada 25°C . Bagi sel suria ITO/b-Si/NiO heterosentuh asimetri bebas dopan (DASH), ketumpatan arus litar pintas (J_{sc}) $4.2 \mu\text{A/cm}^2$, voltan litar terbuka (V_{oc}) 747 mV, faktor isi (FF) 48% dan kecekapan (EFF) $2.3 \times 10^{-3}\%$ telah dihasilkan. Ini melebihi prestasi sel suria rujukan ITO/c-Si/NiO DASH yang mencapai J_{sc} , V_{oc} , FF dan EFF masing-masing $3.6 \mu\text{A/cm}^2$, 721 mV, 34% dan $1.9 \times 10^{-3}\%$. Untuk sel suria organik/inorganik hibrid, sel suria PEDOT:PSS/hibrid menunjukkan J_{sc} , V_{oc} , FF dan EFF masing-masing pada $450 \mu\text{A/cm}^2$, 255 mV, 21% dan $6.0 \times 10^{-2}\%$. Dari segi J_{sc} , FF dan EFF, sel suria PEDOT:PSS/hibrid mengatasi prestasi PEDOT:PSS/c-Si sel suria rujukan yang menunjukkan J_{sc} , V_{oc} , FF dan EFF masing-masing pada $9.03 \mu\text{A/cm}^2$, 368 mV, 14% dan $1.0 \times 10^{-3}\%$. Tindak balas rendah kesemua sel suria adalah disebabkan oleh kehilangan akibat pembayangan yang tinggi dari jejari logam bahagian depan dan sensitiviti peranti yang lemah kerana pencahayaan dari sistem simulator berasaskan LED cahaya putih.

FABRICATION AND CHARACTERIZATION OF BLACK SILICON FOR HETEROJUNCTION SOLAR CELLS

ABSTRACT

Black silicon (b-Si) is a promising technology that reduces broadband reflection within 300-1100 nm wavelength region and improves light absorption in crystalline silicon (c-Si). B-Si consists of a surface with random nanowires or a combination of nanowires and microtextures (hybrid textures) which leads to a refractive index grading effect at the air/c-Si interface. In this work, electroless metal-assisted chemical etching (MACE) is used to fabricate b-Si. One-step MACE, two-step MACE and hybrid microtextures/nanotextures investigating different effects such as etching time, etchants concentration, silver nanoparticles (Ag NPs) layer thickness towards surface morphological and optical properties (within 300-1100 nm wavelength region) of the b-Si are carried out. Two step MACE involve shorter $\text{AgNO}_3\text{:HF}$ dip time. The hybrid texturing involves prior etching in NaOH to produce pyramids. For one-step MACE, nanowires with an average length of $\sim 2.9 \mu\text{m}$ and an average diameter of $\sim 120 \text{ nm}$ are demonstrated. Weighted average reflection (WAR) of 6.0% has been realized. For two-step MACE, nanowires with an average length of 577 nm and diameter of $\sim 200 \text{ nm}$ are produced with WAR of $\sim 5.5\%$. For hybrid textures, nanowires with lengths between 450-600 nm have been obtained on the pyramids with base widths of 3-12 μm and heights of 3-8 μm . The nanowires have lateral width of 30-40 nm. WAR of $\sim 7.2\%$ is obtained. For solar cell fabrication, p-type b-Si is used for ITO/b-Si based heterojunction solar cells and n-type b-Si is used for PEDOT:PSS/b-Si based heterojunction solar cells. Current-voltage

characterization of the solar cells is carried out under white light LED-based (wavelength of 400-800 nm) solar simulator with illumination intensity of 47 mW/cm² at 25°C. For the ITO/b-Si/NiO dopant-free asymmetric heterocontacts (DASH) solar cell, short-circuit current density (J_{sc}) of 4.2 $\mu\text{A}/\text{cm}^2$, open-circuit voltage (V_{oc}) of 747 mV, fill factor (FF) of 48% and efficiency of $2.3 \times 10^{-3}\%$ have been demonstrated. These results outweigh the reference planar ITO/c-Si/NiO DASH solar cell's performance, which achieves J_{sc} , V_{oc} , FF and EFF of 3.6 $\mu\text{A}/\text{cm}^2$, 721 mV, 34%, and $1.9 \times 10^{-3}\%$ respectively. For the hybrid organic/inorganic solar cells, the PEDOT:PSS/hybrid solar cell demonstrates J_{sc} , V_{oc} , FF and EFF of 450 $\mu\text{A}/\text{cm}^2$, 255 mV, 21% and $6.0 \times 10^{-2}\%$ respectively. In terms of J_{sc} , FF and EFF the PEDOT:PSS/hybrid solar cell outweighs the performance of the reference planar PEDOT:PSS/c-Si solar cell which shows J_{sc} , V_{oc} , FF and EFF of 9.03 $\mu\text{A}/\text{cm}^2$, 368 mV, 14% and $1.0 \times 10^{-3}\%$ respectively. The overall low response of the solar cells is attributed to the high shading loss from the front metal fingers and weak device sensitivity due to the illumination from the white light LED-based simulator system.

CHAPTER 1

INTRODUCTION

1.1 Introduction

Research efforts into renewable energy from photovoltaics (PV) materials and devices (PVMD; materials and devices for converting sun energy to electrical energy) have been steadily increasing over the past decades. This is supported by the recent milestones in solar cell efficiency reported by research groups around the world using a variety of materials, fabrication processes and device architectures (Figure 1.1) [2]. After the first PV discovery in 1839 by French physicist Edmund Becquerel achieved by immersing platinum electrodes (referred to as “*Metal Blades*” there in) into an acidic solution and illuminating the solution with light, which resulted a measurable current and voltage [3], in 1941 Russell Ohl reported the first crystalline silicon (c-Si) solar cell [4,5]. Later in 1954, first c-Si solar cell with power conversion efficiency (EFF) of 6% was fabricated in America at Bell laboratories by G.L Pearson, Daryl Chapin and Calvin Fuller [6]. By around 1975 to late 1980’s (as also seen from Figure 1.1) more than 20% efficient c-Si solar cells and gallium arsenide (GaAs) based types were already reported. To this end, solar cells that can convert up to 46% of solar energy into electricity by employing different techniques are fabricated. If this linear trend in (Figure 1.1) is maintained, EFF greater than 40% under standard test conditions (STCs) can be achieved by the end of 2021. To achieve high EFF, there is a need to minimize the electrical losses and increase the amount of incident light that can be effectively absorbed in the active absorber materials by suppressing the surface reflection. This can be done either via an enhanced light scattering at the absorber surface or via diminishing the discontinuity gap of refractive index between material

absorber surface and the surrounding air media [7]. Similarly, this can also be achieved by allowing the collection of illuminated solar light photons with large angles [7].

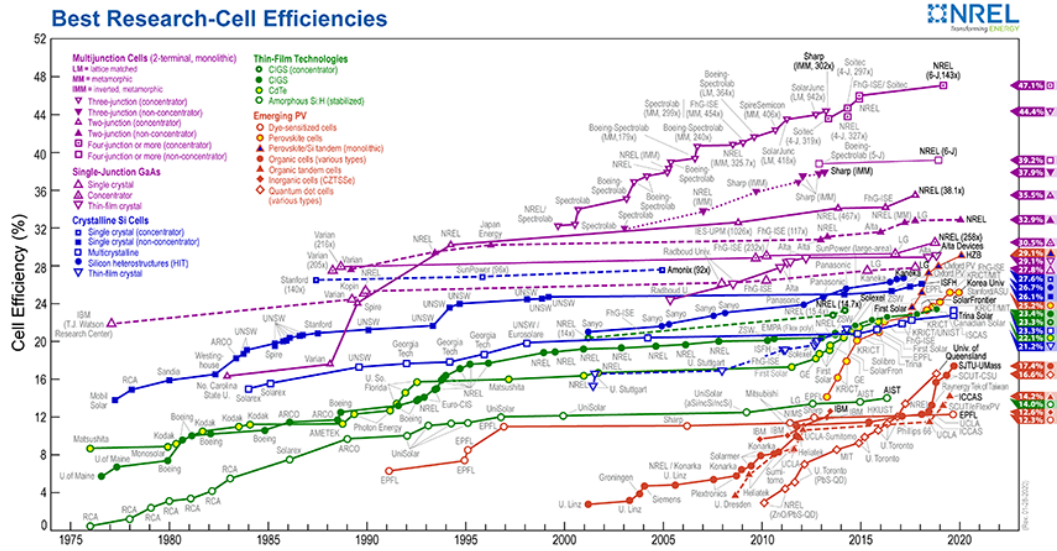


Figure 1.1 NREL solar cell efficiency chart [2].

From Figure 1.1, it is therefore satisfied that PV energy generation with c-Si as the dominant row material with about 90% market share for that purpose is the most promising field among various arena of renewable energy generation using PVMD. The c-Si domination owes to the abundance of silicon dioxide (SiO_2), technology maturity, non-toxicity, and economies of scale [8]. Besides, increasing conversion efficiency (which is around 26% as at late 2020) and reducing technology cost (which is about \$0.24/Watt) further renders the c-Si-based solar cells to be more appealing to the market [8]. Despite the dominance and high market share in the PV market, poor light absorption owing to the indirect bandgap and low absorption coefficient of the c-Si remains a significant challenge for the c-Si solar cells [8]. The poor light absorption of the planar c-Si absorber is due to the high reflection of incident photons (which is about 35-40%) within the 300-1100 nm wavelength region (Figure 1.2 (a)) [9,10]. High reflection of incident photons is undesirable for an efficient PV conversion

process and achievement of high photocurrent in the solar cells. C-Si solar cells can achieve an improved PV conversion by reducing the broadband reflection and increase the amount of incident light that can be effectively absorbed within the active c-Si absorber material [9,10]. C-Si absorber material can achieve a reduction in broadband reflection either via enhanced light scattering at the c-Si absorber surface or via diminishing the refractive index's discontinuity gap between the c-Si absorber surface and the surrounding media [10-12].

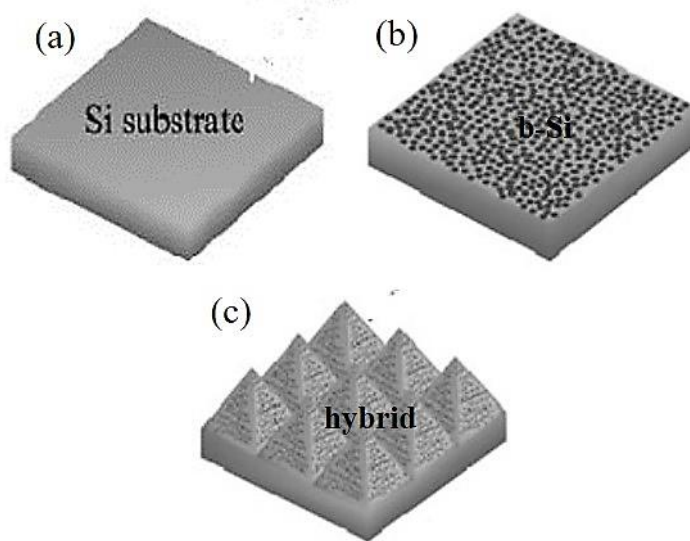


Figure 1.2 Schematic images of: (a) planar reference c-Si, (b) nanotextured and (c) hybrid textured wafers [15].

In the literature, different types of micro-sized surface textures such as random upright pyramids, inverted pyramids and surface groove textures have offered to reduce the surface reflection and increase light absorption of the c-Si absorber [11,12]. However, reducing the broadband reflection from the c-Si absorber to lower than 10.0% using micro-sized surface textures is still challenging and unrealizable. Depositing 80 nm of anti-reflective coating (ARC) on top of the micro-sized surface textures (e.g. silicon nitride (SiN_x), titanium dioxide (TiO_2) or indium tin oxide (ITO)) is usually adopted to address the challenge. Nevertheless, the ARC only suppresses

the reflection to the lowest value at a selective wavelength of around 600 nm. Besides, the process step adds to the manufacturing cost of the solar cells [13,14].

Alternatively, surface nanotexturing to realized nanotextures on the c-Si wafer surface can reduce the surface reflection to lower than 10.0%. The surface nanotextures provide an excellent light trapping effect for a wide angle of incidence when incorporated on the c-Si. Light trapping effect leads to improved light absorption and increased photocurrent, hence power conversion efficiency (EFF) of the solar cells. Nanotexturing produces nanotextures with dimensions smaller than the wavelength of the incident photons (Figure 1.2 (b)) [16,17]. Nanotextures can be porous structures, nanospikes, nanocones, nanowires or nano-hillocks. Another form of promising texturing involves a combination of nanotextures and microtextures on the surface of the c-Si wafer, which is called hybrid textures (Figure 1.2 (c)) [15].

The suppressed reflection due to the presence of surface textures in both nanotextured and hybrid textured c-Si absorbers causes the wafer to appear black to naked eyes compared to un-textured planar c-Si, hence called “black silicon” (b-Si) [18,19]. In a nanotextured b-Si, when the sizes of the nanotextures are smaller than the wavelength of the incident photons (Figure 1.3 (a)), light coupling into the c-Si absorber is realized via the refractive index (n) grading effect [18,19]. The incident light perceives the nanotextures as a medium having a refractive index between ($n_{Si} > n_{NW} > n_{Air}$) that of air media ($n = 1.0$) and that of bulk c-Si ($n = 3.8$) [20]. Conversely, in a hybrid textured b-Si, when the sizes of the nanotextures on the pyramids are smaller than the wavelength of the incident photons (Figure 1.3 (b)), light coupling into the c-Si absorber is realized via the refractive index grading effect by the nanotextures coupled with light scattering by the underlying pyramids [15,21,22]. With surface nanotextures or hybrid microtextures/nanotextures on the c-Si surface,

surface reflection from the c-Si absorber can be suppressed to less than 10% without depositing any other ARC on top of the nanotextures or hybrid textures [22,23]. Moreover, the nanotextures and hybrid microtextures/nanotextures surfaces can provide excellent light trapping for different angles of incidence of the incident photons. This is essential for sunrise-to-sunset applications [15,23,24].

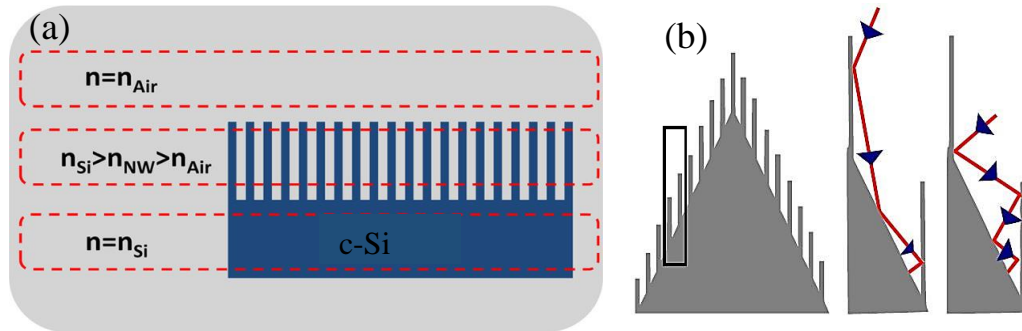


Figure 1.3 Light trapping mechanisms in: (a) nanotextured and (b) hybrid microtextures/nanotextures b-Si [24,25].

B-Si possesses some few unique characteristics not found in bulk c-Si, making it an ideal candidate absorber material for solar cell application: Light trapping and anti-reflection, which can be exploited to allow ARC layers to be fabricated, modified bandgaps controlled by impurity doping, which can be employed to design multi-junction solar cells, low mechanical strength, which can be used to easily separate ultra-thin wafers from silicon ingots, gettering effects, the results of large and active surfaces, which can be utilized to reduce impurities in the wafer [16,19]. B-Si can be fabricated mainly through reactive ion etching (RIE), laser irradiation (LI) and plasma immersion ion implantation (PIII) [19]. At present, these approaches are somehow not applicable for large scale production (industrialization). The non-industrialization of RIE, LI, or PIII-based b-Si for solar cells is due to the requirement of high-tech equipment and more timely processing procedures, which may lead to b-Si solar cells at a high cost per unit watt (\$/W). Metal assisted-chemical etching (MACE) of c-Si is a much more straightforward, promising, and low-cost approach to produce the b-Si

[19]. MACE process does not require high-tech equipment or lengthy processing procedures. The most commonly used catalysts for MACE include silver (Ag), gold (Au) and copper (Cu). B-Si solar cells fabricated with b-Si produced using Au and Cu-based metal catalysts suffer from high recombination losses [24,25]. The high recombination originates from the Au or Cu metal traces which acts as recombination sites in the solar cells. In this work, Ag metal is chosen as a catalyst for the requirement of lower recombination losses in the b-Si solar cells.

At present, the dominant production method of conventional c-Si homojunction solar cells mainly includes aluminium back surface field (Al-BSF) and a phosphorus-doped n⁺ emitter (Figure 1.4 (a)) usually produced by a high-temperature (850°C-900°C) diffusion process [26]. A firing process forms Al-BSF after depositing Al paste at the rear side of a solar cell. Al-BSF process results in a highly doped p-type (p⁺ BSF) region that is conductive to holes and not highly conductive to electrons. BSF (P⁺⁺) role is to form barrier to minority carriers (electrons) flow to the rear contacts and reduce recombination at the rear. The front emitter is usually heavily-doped (with a doping level of $5 \times 10^{19} \text{ cm}^{-3}$) to ensure low sheet resistance and good ohmic contact formation between c-Si and the front metal contacts. Unfortunately, this produces a “dead layer” in the emitter, which leads to poor carrier collection from short wavelength region (300-500 nm), enhanced Auger recombination, bandgap narrowing and free carrier absorption in the solar cells [26]. Furthermore, high carrier recombination losses at the metal/c-Si interface regions limit the performance of Al-BSF doped homojunction c-Si solar cells. At metal/c-Si interfaces, metals induce large densities of electronic states within the bandgap of c-Si, which results in >50% recombination losses in the solar cells [26,27].

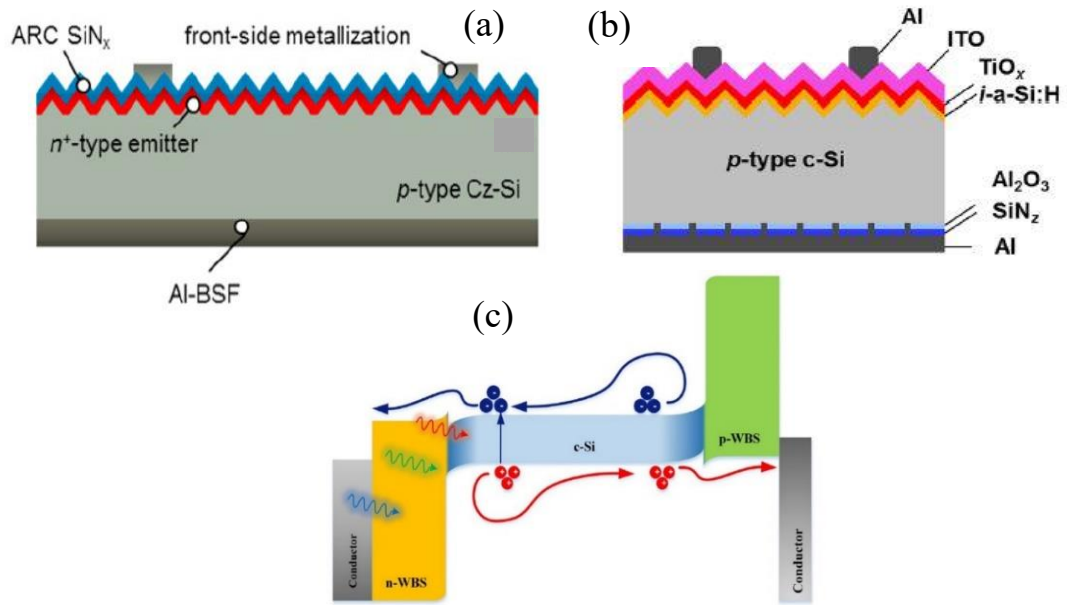


Figure 1.4 C-Si solar cells; (a) Al-BSF homojunction (b) TCO/p-type c-Si heterojunction and (c) DASH heterojunction solar cell concept [26,28,29].

An alternative approach to realize a c-Si solar cell without a high-temperature diffusion process is via the application of a thin film of transparent and conductive oxides (TCOs) like indium tin oxide (ITO); $\text{In}_2\text{O}_3:\text{Sn}$, titanium oxide (TiO_2) or zinc oxide (ZnO) on p-type c-Si [28]. The TCO layer acts as an n-type emitter and produces a simple heterojunction solar cell (see Figure 1.4 (b)). In the TCO/p-type c-Si solar cell, high energy photons in the ultraviolet (UV) region are absorbed by the TCO. Simultaneously, the bulk c-Si absorbs middle and low energy photons in the visible and near-infrared regions. Furthermore, in the TCO/p-type c-Si heterojunction solar cell, a larger energy bandgap of the TCO with respect to c-Si (1.12 eV) results in lower reverse saturation current density (J_0) due to lesser defects at the interface. Lower J_0 results in suppressed interface recombination, which yields higher V_{oc} than Al-BSF doped homojunction c-Si solar cells [28,29]. Interface passivation materials (e.g. SiO_2 , intrinsic hydrogenated amorphous silicon (i-a-Si:H), SiN_x , or aluminium oxide

(Al_2O_3) are usually applied to further suppress recombination of charge carriers at the interfaces of TCO/p-type c-Si. In this type of solar cell, the work function of the ITO, TiO_2 or ZnO layer causes an inversion at the interface of the c-Si substrate and hence a simple p–n junction is formed [28].

Poly(3,4-ethylene dioxythiophene)–poly(styrene sulfonate) (PEDOT:PSS) shows similar properties when deposited on n-type c-Si [28,30]. In this concept, the observed behaviour is due to the native n-type conductivity of TCO and p-type conductivity of PEDOT:PSS coupled with Schottky barrier formation when either TCO or PEDOT:PSS is in contact with the c-Si [27,30]. The overall advantage of TCO/p-type c-Si or PEDOT:PSS/n-type c-Si heterojunction solar cell is eliminating dead layer issues on the front side of the conventional Al-BSF doped homojunction c-Si solar cell introduced earlier. Avoidance of the high-temperature diffusion process is another merit of the TCO/p-type c-Si and PEDOT:PSS/n-type c-Si heterojunction solar cells.

Furthermore, the development of c-Si heterojunction solar cells using passivating contacts yielded promising results [27,31]. The technology is known as heterojunctions with intrinsic thin passivation layers (HIT; a-Si:p/i-a-Si:H/n-c-Si/i-a-Si:H/a-Si:n). However, the parasitic absorption of the incident photons within the doped a-Si:H layer has been a challenge in this technology [27,31]. Besides, materials with low work function or high work function having suitable band alignment with c-Si are intensively being investigated as dopant-free asymmetry heterocontacts (DASH) for solar cells and as substitutes of doped a-Si:n and a-Si:p, as illustrated in Figure 1.4 (c) [32,33].

The DASH solar cells concept involves introducing an asymmetric band alignment configuration at the c-Si and contacts material interfaces to block transport

of one type of charge carrier while allowing free passage of another carrier type [31-33]. Substituting the doped amorphous silicon (a-Si:(n or p)) film at the front of amorphous silicon/c-Si heterojunction solar cells with wide-bandgap transition metal oxides (TMOs (oxides of metals from group 1 and 2 in the periodic table)) was proven to mitigate parasitic light absorption losses by improving optical performance while still maintaining excellent passivation and high FF reported while replacing p-type amorphous silicon with thin films of either molybdenum oxide (MoO_x), vanadium oxide (V_2O_5), nickel oxide (NiO) or tungsten oxide (WO_3).

Continuously, combination of compound materials from TMOs, metal nitrides, alkali metals halides and their carbonates are been explored for the asymmetric carrier selectivity as carrier selective contacts (CSCs) in the DASH solar cells. Of interest within these materials are TMOs [31-33]. High work function TMOs having a small valance band offset with c-Si (as shown in Figure 1.5) has been investigated as hole selective contacts and replacement for a-Si:p thin layer in amorphous silicon-based heterojunction solar cells [31-33].

TMOs materials with low work function and a small conduction band offset with c-Si like TiO_2 , ZnO, ZnO:Al (AZO), ZnO:B (BZO), MgO_x , TaO_x , TaN_x , LiF,) have been demonstrated as electron-selective contacts and replacement for a-Si:n thin layer [32,33]. For DASH solar cells featuring TMOs as CSCs, carrier extraction is achieved via band bending in c-Si resulted when it is contacted by high or low work function CSCs.

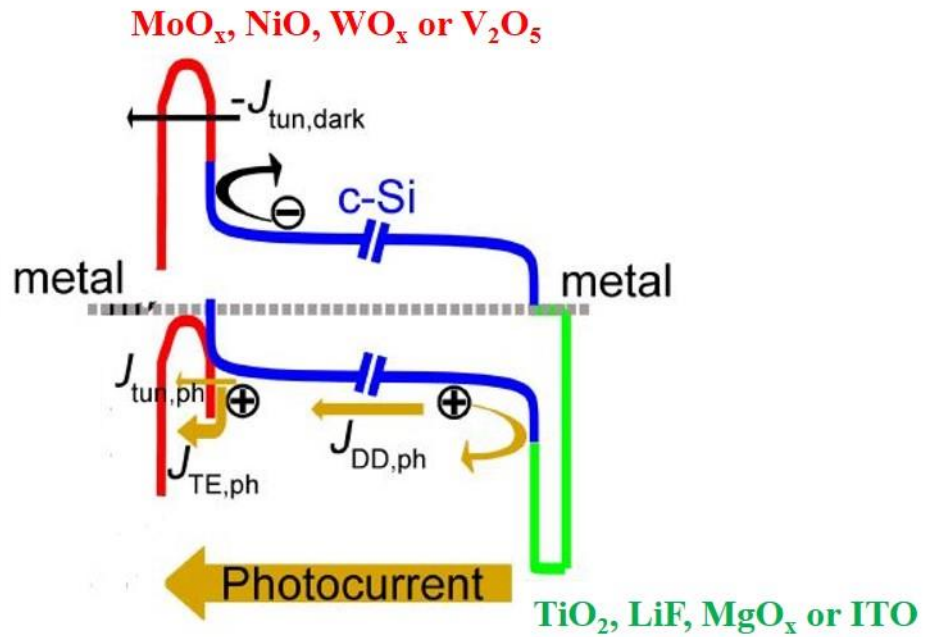


Figure 1.5 Energy band diagram of DASH solar cell featuring TMOs under short-circuit condition. The TMOs form heterojunctions with c-Si at the opposite ends and provide selective contacts for holes and electrons, respectively. Components of dark, tunnelling and thermionic emission currents are identified on the band diagram. The diagram is not drawn to scale.

Figure 1.5 shows that low conduction band offset between c-Si and TMOs is responsible for electron transport and high valence band offset being responsible in making a barrier for holes (implying low carrier recombination) transport from c-Si to TMOs. Besides, electron-selective titanium dioxide (TiO_2) and hole-selective molybdenum oxide (MoO_x) contacts have successfully replaced a-Si:n and a-Si:p, respectively in HIT (a-Si:p/i-a-Si:H/n-c-Si/i-a-Si:H/a-Si:n) [33]. Easy and simple deposition techniques like magnetron sputtering, atomic layer deposition (ALD), spin coating and thermal evaporation are used to deposit CSC, TCO and PEDOT:PSS at a lower temperature compared to Al-BSF doped homojunction c-Si solar cells. The ease in deposition processes of CSC, TCO and PEDOT:PSS for the fabrication of heterojunction solar cells will translate to low-cost solar cells.

1.2 Problem statement

Despite the domination of c-Si solar cells in the PV market, the poor light absorption of planar c-Si (see Figure 1.6 (a)) due to high surface reflection (35-40%) of incident light within 300-1100 nm wavelength region has been a major issue with the solar cells. The high surface reflection means only 60-65% of the incident light is absorbed by the c-Si, as illustrated in Figure 1.6 (b). Besides, the poor light absorption is attributed to the indirect bandgap and low absorption coefficient of the c-Si absorber. Suppression of the high surface reflection in the c-Si can be realized using a b-Si absorber (see Figure 1.6 (c)) and has been outlined as a way forward to increase the performance of the c-Si solar cells [34].

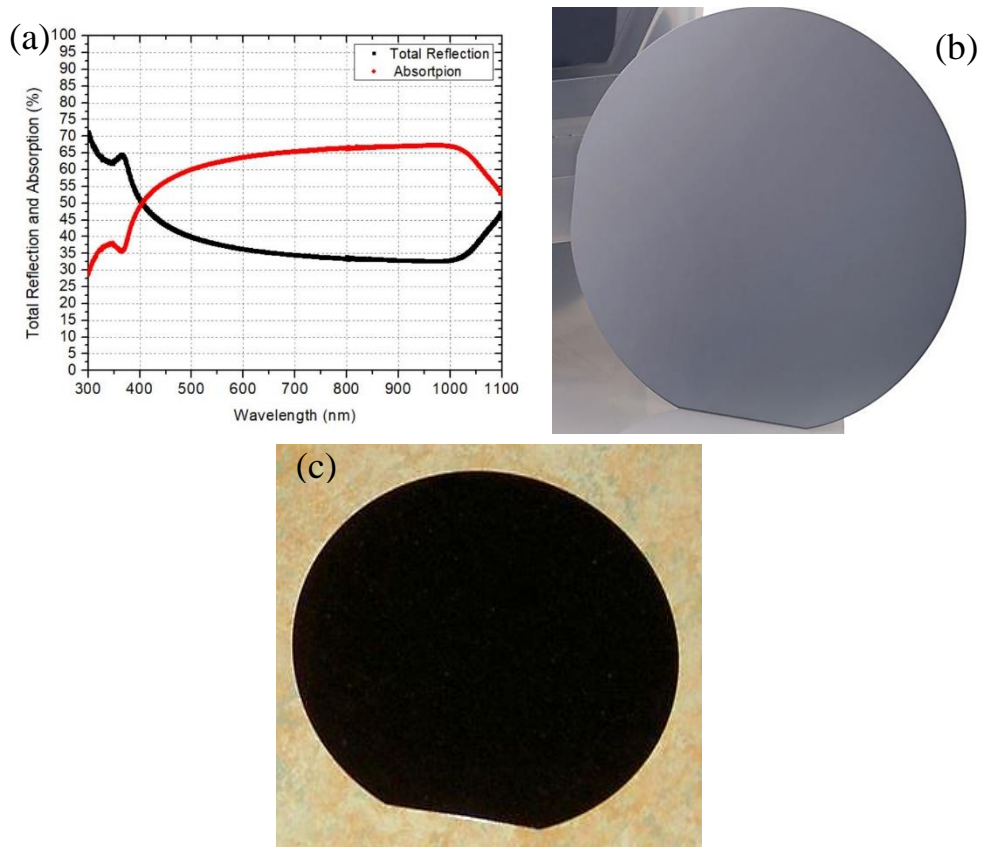


Figure 1.6 (a) Total reflection and absorption of planar c-Si within 300-1100 nm wavelength region (b) Planar c-Si (c) B-Si [34].

At present, b-Si (nanotextures or hybrid textures (microtextures/nanotextures)) can be fabricated using MACE process. However, the existing MACE approaches involve a long process, ranging from few minutes to few hours, and produce b-Si nanotextures with lengths of around 1-6 μm [2,7,16-18,21,23-25,35-44]. Such long nanotextures exhibit high surface recombination due to the nanotexture's high aspect ratio, which yields low PV response in the b-Si solar cells [22,24,35-44]. Furthermore, long processing procedures are not applicable for industrial scalability. Thus, optimizing the fabrication method for realization of optimized b-Si nanotextures on the c-Si with shorter lengths (below 1 μm) using a shorter process duration is crucial. Besides, the developed b-Si should also exhibit low broadband reflection within 300-1100 nm wavelength region, so that short-circuit current density (J_{sc}) of the b-Si solar cells is not compromised. Thus, the development of b-Si using a shorter process duration which exhibit low broadband reflection within 300-1100 nm wavelength region is outlined as the important research gap the thesis aims to address.

In conventional Al BSF doped homojunction c-Si solar cells, the front emitter is heavily-doped (around $5 \times 10^{19} \text{ cm}^{-3}$) to ensure low sheet resistance and good ohmic contact. However, the high doping level produces a “dead layer” in the emitter. The “dead layer” leads to poor collection of charge carriers from short wavelength region (300-500 nm), enhanced Auger recombination, bandgap narrowing and free carrier absorption in the Al BSF doped homojunction c-Si solar cells [36,37]. High carrier recombination losses at the metal/c-Si interfaces also limit the performance of Al-BSF doped homojunction c-Si solar cells as earlier introduced. Thus, TCO/p-type c-Si, PEDOT:PSS/n-type c-Si and DASH concepts of heterojunction solar cells offer a promising solution. However, in a typical planar TCO/p-type c-Si featuring ITO emitter (referred as ITO/c-Si onward) or in a PEDOT:PSS/n-type c-Si (referred as

PEDOT:PSS/c-Si onward) heterojunction solar cell, photon absorption at the front ITO or PEDOT:PSS emitters is only efficient at specific wavelengths and depends on the incidence angle of the incident photons [45-48]. Dependence of photon absorption on wavelength is because the ITO and PEDOT:PSS present spectral changes in photon absorption according to the principle of quarter-wavelength for ARC design ($nd=\lambda/4$) [45-48]. The dependence of photon absorption on the principle of quarter-wavelength for ARC design will limit the performance of the heterojunction solar cells. Therefore, depositing the front ITO or PEDOT:PSS emitter on the b-Si absorber with nanowires of average heights smaller than $\sim 1 \mu\text{m}$ may guarantee a significant enhancement in light absorption.

Therefore, the thesis will investigate one-step MACE, two-step MACE and hybrid (microtextures/nanotextures) texturing methods to fabricate b-Si with nanowires of average heights smaller than $\sim 1 \mu\text{m}$ within a short duration (30-60 s) for novel solar cell architecture based on DASH concept, featuring ITO emitter and nickel oxide (NiO) hole contact (i.e. ITO/b-Si/NiO compared to ITO/c-Si/NiO). Besides, the thesis will also investigate PEDOT:PSS/b-Si heterojunction solar cells in comparison to planar reference PEDOT:PSS/c-Si cell.

1.3 Objectives

The objectives of this work are as the following:

1. To develop one-step, two-step and hybrid textures based on electroless metal-assisted chemical etching (MACE) for fabrication of b-Si.
2. To investigate surface morphology, optical and electrical properties of ITO and PEDOT:PSS as emitter layers on b-Si.

3. To assess the photovoltaic performance of ITO/b-Si and PEDOT:PSS/b-Si heterojunction solar cells.

1.4 Thesis outline

This thesis is divided into five chapters. **Chapter 1** explains the motivations behind the research on b-Si for heterojunction solar cells. The chapter also introduces the importance of light trapping in c-Si solar cells. The need for light trapping in heterojunction solar cells (ITO/b-Si and PEDOT:PSS/b-Si heterojunction solar cells) is also highlighted.

Chapter 2 contains the review of related literature and theoretical background information on which the thesis is based. The reviewed related literature cover roles of light trapping in c-Si solar cells right from the concept of Yablonovitch limit (Lambertian scatter) and electroless MACE approaches to incorporate b-Si nanotextures into c-Si solar cells. The general principles and theories of b-Si light-trapping properties for applications in solar cells are discussed. At the end of the chapter, possibilities, attempts and highlights of incorporating b-Si nanotextures in to TCOs/c-Si heterojunction, DASH solar cells and PEDOT:PSS/c-Si heterojunction solar cells are presented.

Chapter 3 presents the detailed description of the methodology used in this work. These include the experimental fabrication procedures of b-Si nanowires, hybrid (microtextures/nanotextures) surfaces and ITO/b-Si/NiO DASH and PEDOT:PSS/b-Si heterojunction solar cells. Fabrication and characterization equipment in NOR lab utilized in this work to study the properties of b-Si nanowires, hybrid (microtextures/nanotextures) surfaces, PEDOT:PSS/b-Si, ITO/b-Si heterojunction interfaces and heterojunction solar cells are discussed in the chapter.

Chapter 4 presents the results of b-Si (nanowires/hybrid (microtextures/nanotextures)) from one-step MACE and two-step MACE processes including the effect of process parameters on b-Si formation. Absorption enhancement achieved in the b-Si nanowires and hybrid (microtextures/nanotextures) textured surfaces compared to reference planar c-Si are investigated and discussed. Besides, the chapter presents morphological optical, and electrical properties of ITO/b-Si and PEDOT:PSS/b-Si hetero interfaces. Electrical parameters of the fabricated heterojunction solar cells are also presented in the chapter.

Chapter 5 concludes the whole thesis and summarizes the findings and original contributions to the knowledge of b-Si. The chapter also outlines recommendations for future works.

1.5 Original contributions

From this thesis, the author's main contributions to the field of b-Si for solar cells are as the following:

- Developed a novel fabrication method of b-Si nanowires using one-step MACE process in aqueous solution of HF:AgNO₃ (without involving another oxidizer such as H₂O₂) with etching duration of 60 to 90 s. The process produces b-Si nanowires of about 2-3 μm height and 120 nm diameter which result in WAR of 6.0% within 300-1100 nm wavelength region.
- Developed a two-step MACE process involving a short process duration (10-25 s) in HF:H₂O₂ solution after 30 s of Ag NPs deposition in AgNO₃:HF. The process results in b-Si nanowires of ~577 nm length and 206 nm average diameter with WAR of ~5.5% within 300-1100 nm wavelength region.

- Investigated the effects of Ag NPs layer thickness towards formation of b-Si nanowires based on two-step MACE process.
- Developed a method of fabricating nanowires on pyramids within shortest possible duration (20 s of etching after 30 s of Ag NPs deposition) which is crucial for process scalability. Hybrid (microtextures/nanotextures) textured surfaces are fabricated and investigated to increase broadband light absorption (within 300-1100 nm wavelength region) in c-Si absorbers.
- Investigated morphological and optical properties of DC magnetron sputtered ITO thin films on b-Si. Further experiments that investigated the effects of different annealing temperatures (200°C-500°C) on the properties of the sputtered ITO thin films on the b-Si are also reported.
- Demonstrated novel ITO/b-Si/NiO heterojunction solar cell which achieves high V_{oc} (747 mV) and enhanced J_{sc} in comparison to reference ITO/c-Si/NiO cell.

CHAPTER 2

LITERATURE REVIEW AND THEORETICAL BACKGROUND

2.1 Introduction

This chapter presents a review of related literature on black silicon for application in solar cells. The Chapter reviews various works reporting b-Si fabrication based on laser irradiation, PII, RIE and MACE techniques. Theoretical background on the operation of standard p-n junction solar cells and refractive index grading effect are also presented in the Chapter.

When the surface of c-Si is textured such that nanotextures are formed on its surface, which makes it appear black to naked eyes as earlier introduced, the resulting material is generally called b-Si in the literature [49,50]. The discovery of textured c-Si based on MACE technique via micro contamination of Ag onto p-type c-Si (111) in a solution of $0.01 \text{ mol L}^{-1} \text{ AgNO}_3$ at room temperature was first reported by Morinaga et al. in 1994 [19]. However, Morinaga et al. have not achieved fully textured b-Si material, fully textured b-Si material was first accidentally discovered by Mazur et al. in 1996 at Harvard University in Cambridge and later announced to the world at the American Physical Society Centennial meeting in 1999 in Atlanta, Georgia [51]. Mazur et al. placed a c-Si wafer in a vacuum chamber that was filled with chalcogen-containing gas and irradiated the c-Si wafer with ultrashort pulses from a femtosecond laser. The c-Si wafer turns to appear black to naked eyes after the experiment. The wafer appears black because the reflection of visible light is virtually zero. Upon examination, the team discovered the blackened surface was covered with a vast array of nanoscale spikes. The blackness of this material depends on the sizes, length, aspect ratio and shape of the formed nanoscale spikes. Several works on b-Si fabrication for solar cells applications other techniques have then emerged. This project gives emphasis

on MACE based b-Si for such applications. Thus, Table 2.1 summarizes properties of b-Si fabricated using MACE process which include synthesis methods, etchants composition, etching time, nanotexture types, length of nanotextures, WARs and EFF achieved in some fabricated b-Si solar cells reported in the literature for benchmarking. From the table, it is clear light trapping in heterojunction and DASH solar cells is relatively less explored. The less exploration of light trapping in such configurations of solar cells justify another reason why this project considers exploring b-Si light trapping in heterojunction solar cells.

Table 2.1 Literature status of MACE-based b-Si: Synthesis methods, etchants composition, etching time, nanotexture types, length of nanotextures WARs and EFF achieved.

Synthesis Method	Etchants Composition	Etching Time (min/s)	Texture type	Length (Depth) (nm)/(μm)	WAR (%)	Cell type	EFF (%)	Refs.
Two-step MACE	5% HF: 0.02 M AgNO ₃ / 4.8M HF: 0.2M H ₂ O ₂	60 s/15 min	Nanowires	4 μm	1.5	-	-	[9]
One-step MACE	AgNO ₃ 0.06 M: HF 3.0 M	2.5 min	Nanowires	1 μm	7.5	-	-	[14]
Two-step MACE	5M HF: 20 mM AgNO ₃ 10 % HF: 0.6 % H ₂ O ₂	60 s/60 min	nanocone arrays	2.5 μm	7.0	homo	-	[16]
Two-step MACE (hybrid)	4 mM AgNO ₃ : 0.5 vol% HF + 12.5 vol% HF: 3 vol% H ₂ O ₂ : DI H ₂ O	90 s/20 s	nanoholes on pyramids	300 nm	2.9	hetero	9.96	[15]
One-step MACE	4.6 M HF: 0.02 AgNO ₃	20 min	Nanowires	1.5 μm	-	hetero	5.6	[18]
Lithography + Two-step MACE	50 nm thick Au film + HF: H ₂ O ₂ etch	25 min O ₂ NSL etch and 180 s MACE	Nanospheres	590 nm	10.0	-	-	[21]

Synthesis Method	Etchants Composition	Etching Time (min/s)	Texture type	Length (Depth) (nm)/(μm)	WAR (%)	Cell type	EFF (%)	Refs.
Two-step MACE	10 nm Ag film + 5 M HF: 0.44M H ₂ O ₂ etch	30 min	Nanowires	6 μm	-	-	-	[23]
One-step MACE	4.6 M HF: 0.02 AgNO ₃	40 min	Nanowires	1.7 μm	9.9	homo	14.4	[24]
One-step MACE (hybrid)	5 M HF: 30 mM AgNO ₃	15 min	nanowires on pyramids	~2 μm	~3.0	-	-	[25]
One-step MACE (hybrid)	0.4 mM HAuCl ₄ + HF: H ₂ O ₂ : H ₂ O (1:5:2)	3 min	nanopores on pyramids	450 nm	~2.0	homo	17.1	[35]
One-step MACE	4.6 M HF: 0.02 AgNO ₃	20 min	Nanowires	~5 μm	~2.0	homo	9.31	[36]
One-step MACE	HF/Fe(NO ₃) ₃	50 min	Nanowires	~5 μm	1.46	-	-	[37]
One-step MACE (hybrid)	3 M HF: 0.06 M AgNO ₃	3 min	nanowires on pyramids	~500 nm	~3.0	homo	11.12	[38]
One-step MACE	20 mM AgNO ₃ : 14 M HF	10 min	Nanowires	~3.0 μm	3.08	-	-	[39]
One-step MACE	HF (49 wt%): H ₂ O ₂ (28 wt%): AgNO ₃ (10 wt%): H ₂ O (8: 1: 0.018: 32) + (HF (49 wt%): HNO ₃ (69 wt%): H ₂ O (3: 50: 70))	(5 + 2) min	Nanopores	3.66 μm	10.2	homo	19.4	[40]
Two-step MACE	20 nm-thick Ag film + 10% HF: 0.6% H ₂ O ₂ etch	30 min	Nanopores	2.0 μm	-	-	-	[41]
One-step MACE	20 mM AgNO ₃ :HNO ₃ (25 %): HF (20 vol%)	30 min	Nanowires	500 nm	~3.0	homo	9.60	[42]
Two-step MACE (hybrid)	AgNO ₃ :Na ₂ S ₂ O ₈ + HF:H ₂ O ₂ : H ₂ O	6 min/2 min	nanopores on pyramids	200 nm	~3.0	homo	17.5	[43]

Synthesis Method	Etchants Composition	Etching Time (min/s)	Texture type	Length (Depth) (nm)/(μm)	WAR (%)	Cell type	EFF (%)	Refs.
One-step MACE	14 M HF: AgNO ₃	30 min	Nanowires	6.0 μm	-	-	-	[44]
One-step MACE (hybrid)	4 M HF:0.01 M AgNO ₃	500-900 s	nanowires on pyramids	~670 nm	5.77	homo	17.63	[52]
Cu/Ag two-step MACE	(5:1) Cu (NO ₃) ₂ /AgNO ₃ + HF:H ₂ O ₂ (3:10)	-	Nanopores	~ 1 μm	15.52	homo	18.91	[53]
Two-step MACE	HF: AgNO ₃ :Additive + HF:H ₂ O ₂ : H ₂ O	60 s/360 s	Nanopores	1.1 μm	2.3	homo	19.51	[54]
Two-step MACE	4 M HF:0.01 M AgNO ₃ + HF:H ₂ O ₂ : H ₂ O	60 s + 260 s	deep holes	~500 nm	5.62	homo	19.11	[55]
One -step MACE (hybrid)	HF/HNO ₃ /H ₂ O + AgNO ₃ + HF		honeycomb-like structures	3.5 μm	12.10	homo	21.39	[56]
Cu/Ag one-step MACE	5.8 M HF and 0.6 M H ₂ O ₂ + 2.4 mM Cu (NO ₃) ₂ + 0.06 mM AgNO ₃	180 s	Nanopores	~1.0 μm	6.27	homo	19.77	[57]
Two-step MACE	Ag ink + HNO ₃ (70%), HF (50%) etch	450 s	Nanowires	695 nm	1.96	-	-	[58]
Two-step MACE	HF (0.2 M) : AgNO ₃ (3 × 10 ⁻⁵ M) + H ₂ O ₂ (3.13 M) and HF (2.46 M)	7 min	Nanopores	1-3 μm	9.2	homo	20.19	[59]

2.1.1 Light trapping in crystalline silicon solar cells

Section 2.1.1 presents a review of related literature on light trapping in mono c-Si. Micro-texturing, b-Si, and hybrid textures reported by other research groups are reviewed. Light trapping in mono c-Si is crucial to increase optical path length by up

to 50 times the device thickness for the c-Si absorber. An increase in optical path length curtails the impinging challenge of low optical absorption and address the limited diffusion length issue in c-Si solar cells. For a c-Si absorbing material, Yablonovitch et al. reported that with the presence of light-trapping micro-textures, an incident photon would see the c-Si thicker than its actual thickness (d) by around $4n^2$ (i.e. $4n^2 d$, where n is the refractive index of c-Si). Still, in the solar cells, the electron-hole pairs will travel within the c-Si without recombining until they are separated at the junction [60]. Yablonovitch limit was later generalized by Green et al. in 2002 [61].

Fabrication of micro upright pyramids (shown in Figure 2.1) on the mono-c-Si surface is usually achieved via alkaline etching using TMAH, KOH or NaOH solution [62]. Random upright pyramids are formed due to anisotropic etching by the TMAH, NaOH or KOH. The alkaline etchants etch (100) and (110) crystallographic planes of c-Si faster than (111) planes [63]. The concept of alkaline texturing is not applicable for texturing multi c-Si due to the possession of several grains with different crystal orientations on the surface of multi c-Si. Instead, HNO_3 , HF, H_2O_2 mixture solution is used to make random microtextures in the case of multi c-Si (which is beyond the scope of this project).

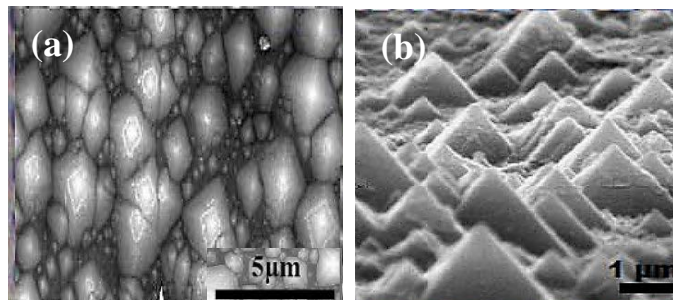


Figure 2.1 Top (a) and cross section (b) FESEM images of pyramidally textured c-Si using NaOH texturing. The scale bar is with 5 μm and 1 μm respectively [62].

Another strategy to trap the photons of incident light in c-Si-based solar cells is by using b-Si nanotextures fabricated using various fabrication methods. Zhong et

al. reported c-Si-based solar cell fabricated with light trapping nanohillocks having an average height of 150–600 nm formed on the c-Si surfaces by PIII texturing [64]. Surface reflection over the wavelength range of 300 nm to 1100 nm has been reported to decrease with increasing the height of nanohillocks. In contrast, the IQE decreases in the final device when the size of the nanohillocks get higher. After optimising the nanohillocks, a height of 300 nm yields a better 15.99% efficient b-Si solar cell [64]. The results have reported that the increase in the nanohillocks area contributes to the easier phosphorous diffusion into the wafer, leading to a decreased sheet resistance (R_{sheet}) which yields the 15.99% efficient b-Si solar cell.

Similarly, Savin et al. fabricated b-Si with nanotextures of ~ 800 nm height. Cryogenic inductively coupled plasma reactive-ion etching process (DRIE; Plasmalab System 100, Oxford Instruments) at -120°C using SF_6 and O_2 as the etching gases is adopted in their work. The results have further used a thick interdigitated back-contact back-junction (IBC) solar cell configuration to achieve b-Si IBC solar cell with an active surface area of 9.0 cm^2 having EFF greater than 22% [65]. Highly conformal atomic layer deposited (ALD) thin films (to make use of combined chemical and field-effect passivation ability of Al_2O_3) passivation is used in their work to show promising results in overcoming the problematic surface recombination issue in b-Si solar cells.

With regards to MACE based b-Si solar cells, Yuan et al. studies optical effects and factors limiting performance efficiency of the fabricated b-Si solar cells that incorporated density-graded nanoporous surface layers made by Ag-based one-step MACE [66]. Fabricated b-Si solar cells that reflect less than 3% of incident photons without the addition of conventional ARC have been reported from the results. The findings showed that the solar cells are limited by recombination in the nanoporous layer. The recombination decreases the short-wavelength spectral response of the solar

cells. The results concluded that the optimum density-graded layer depth is a compromise between reflection reduction and recombination loss. Auger recombination processes caused by the lengthier nanotextures have been reported to be responsible for limiting the photogenerated charge collection and EFF of the b-Si solar cells. Auger recombination arise due to excessive doping related to in-diffusion through the high surface area of the nanostructures. Zhou et al. reported a c-Si solar cell with a b-Si layer made at the rear using one-step Ag-based MACE to develop a c-Si solar cell with sub-bandgap PV response [67]. The results showed that a c-Si solar cell with b-Si nanoarrays of about ~ 110 nm in height at the rear performs better than that of a similar structure without b-Si. Enhancement in EFF by up to about 27.7% was achieved despite the large specific surface area of the b-Si. The results attributed the high EFF to the graded bandgap formed at the rear of the b-Si solar cell. Achievement of graded bandgap as opposed to refractive index grading effect is revealed by contact potential difference (CPD) measurements. CPD measurements show that the conduction band minimum of b-Si is 0.4 eV above that of p-type c-Si. Meaning the bandgap of b-Si is larger than that of p-type c-Si. Thus, the bandgap width of b-Si is larger than that of p-type c-Si thereby forming a graded bandgap since the b-Si is grown on p-type c-Si. From their work, photoluminescence (PL) emission and quantum confinement effect analysis are used to support the graded bandgap observation [67]. After adopting a one-step MACE deep etch process, Kumagai performs Ag-based MACE on c-Si diamond wire sawn wafer using AgNO_3 as the silver source. Kumagai has further presented the possibility of controlling the nanotextures structure by easily changing the immersion time in the etching container [68]. Srivastava et al. reported Ag-based one-step MACE of p-type c-Si (100) substrates in aqueous HF and AgNO_3 , which realizes 50–300 nm large area vertically aligned b-Si nanowires (define as “VA-

SiNW sub-wavelength structures” therein). The results presented that the length of the nanotextures increases linearly with etching time (20–120 min). Remarkable reduction in surface reflection to less than 2% within 300–600nm and less than 4% within 600–1000 nm wavelength range yields improved PV response in the solar cell [69]. Lu et al. reported a room-temperature synthesis of nanopore-type b-Si. The b-Si significantly decreases the surface reflection of c-Si wafer surfaces. Longer etching durations (50 min-12 hours) have been reported to fabricate the b-Si via Ag-assisted one-step MACE [70]. The effects of the Ag catalyst concentration (500, 50, and 5 μM), the HF and H_2O_2 concentration in the c-Si etchant, the HF: H_2O_2 ratio and etching time on the surface morphology and the corresponding surface reflection have been presented in the results. From the findings, the lowest relative surface reflection (0.17% over a range of 300–1000 nm) occurs with an Ag ion concentration of 50 μM . For the Ag concentration of 5 μM , surfaces with a short nanopore length of 250 nm, which achieved a low surface reflection of 2.60%, were obtained. The results have concluded that the b-Si morphology possesses high dependence on the Ag concentration, HF: H_2O_2 : H_2O volume ratio, and the etching time.

With regard to two-step texturing and two-step MACE based processes of texturing c-Si for solar cells application, Oh et al. compare the EFF of an industry-standard ARC coated polished c-Si solar cell and fabricated 18.2% efficient b-Si solar cell without ARC. EFF of 18.6% was achieved by controlling carrier recombination in the nanostructured b-Si by using anisotropic tetramethylammonium hydroxide (TMAH) post-etch after the gold-based two-step MACE [71]. Surface and Auger recombinations have been demonstrated by the results achieved in the nanostructured b-Si solar cells. However, the dominant mechanism (i.e. either surface or Auger recombination) depend on p–n junction formation conditions and the surface area of